An Immune Cell Atlas Reveals Dynamic COVID-19 Specific Neutrophil Programming Amenable to Dexamethasone Therapy

Authors: Sarthak Sinha[1*], Nicole L. Rosin[1*+], Rohit Arora[1], Elodie Labit[1], Arzina Jaffer[1], Leslie Cao[1], Raquel Farias[3,4], Angela P. Nguyen[3,4], Luiz G. N. de Almeida[2,5], Antoine Dufour[2,5], Amy Bromley[6], Braedon McDonald[3,4], Mark Gillrie[3,7,8], Marvin J. Fritzler[3,8], Bryan Yipp[3,4 +], Jeff Biernaskie[1,9,10 +]

Affiliations:

[1] Department of Comparative Biology and Experimental Medicine, Faculty of Veterinary Medicine, University of Calgary;

[2] Department of Physiology & Pharmacology;

[3] Calvin, Phoebe and Joan Snyder Institute for Chronic Diseases, Cumming School of Medicine, University of Calgary;

[4] Department of Critical Care Medicine, Cumming School of Medicine, University of Calgary;

[5] McCaig Institute for Bone and Joint Health, University of Calgary;

[6] Department of Pathology and Laboratory Medicine, University of Calgary;

[7] Department of Microbiology, Immunology and Infectious Diseases, University of Calgary;

[8] Department of Medicine, Cumming School of Medicine, University of Calgary, Calgary, AB, Canada;

[9] Hotchkiss Brain Institute, University of Calgary;

[10] Alberta Children's Hospital Research Institute, University of Calgary

[*] Equal contribution

[+] Corresponding authors

Summary

SARS-CoV-2 is a novel coronavirus that causes acute respiratory distress syndrome (ARDS), death and long-term sequelae. Innate immune cells are critical for host defense but are also the primary drivers of ARDS. The relationships between innate cellular responses in ARDS resulting from COVID-19 compared to other causes of ARDS, such as bacterial sepsis is unclear. Moreover, the beneficial effects of dexamethasone therapy during severe COVID-19 remain speculative, but understanding the mechanistic effects could improve evidence-based therapeutic interventions. To interrogate these relationships, we developed an scRNA-Seq and plasma proteomics atlas (biernaskielab.ca/COVID_neutrophil). We discovered that compared to bacterial ARDS, COVID-19 was associated with distinct neutrophil polarization characterized by either interferon (IFN) or prostaglandin (PG) active states. Neutrophils from bacterial ARDS had higher expression of antibacterial molecules such as PLAC8 and CD83. Dexamethasone therapy in COVID patients rapidly altered the IFN^{active} state, downregulated interferon responsive genes, and activated $IL1R2^{+ve}$ neutrophils. Dexamethasone also induced the emergence of immature neutrophils expressing immunosuppressive molecules ARG1 and ANXA1, which were not present in healthy controls. Moreover, dexamethasone remodeled global cellular interactions by changing neutrophils from information receivers into information providers. Importantly, male patients had higher proportions of IFN^{active} neutrophils, a greater degree of steroid-induced immature neutrophil expansion, and increased mortality benefit compared to females in the dexamethasone era. Indeed, the highest proportion of IFN^{active} neutrophils was associated with mortality. These results define neutrophil states unique to COVID-19 when contextualized to other life-threatening infections, thereby enhancing the relevance of our findings at the bedside. Furthermore, the molecular benefits of dexamethasone therapy are also defined, and the identified pathways and plasma proteins can now be targeted to develop improved therapeutics.

47 **COVID-19 ARDS host responses contextualized to bacterial ARDS.**

48 A broad array of infections including SARS-CoV-2 and bacterial sepsis can induce acute respiratory
49 distress syndrome (ARDS), respiratory failure and death[1-3]. Neutrophils are thought to be key drivers of
50 both COVID-19 and bacterial ARDS[4-6], yet it is unclear if this is related to intrinsic and/or irreversible
51 cellular responses. While recent studies have leveraged single-cell transcriptomics to dissect peripheral[7-
52 9]and bronchoalveolar fluid [10-12]immune landscapes driving COVID-19 pathogenesis, the protocols used
53 can inadvertently exclude the majority of polymorphonuclear granulocytes, including neutrophils, as they
54 are highly sensitive cells with low RNA (and high RNase) content. Here, we employ whole-blood-
55 preserving protocols that capture all major immune cell types from critically ill patients admitted to
56 intensive care units (ICUs) (Extended Fig 1). All samples taken from COVID-19 patients were assessed
57 by bacterial culture and tested negative. All COVID-19 patients tested positive by PCR for SARS-CoV-2,
58 and we previously confirmed an absence of viral mRNA in any circulating immune cells in a subset of
59 patients[13]. However, a plasma proteomic screen for SARS-CoV-2 specific viral proteins in all samples
60 revealed detection of one or more viral proteins in COVID-19 patient serum (Extended Fig 2a).
61 Furthermore, we compared patient samples from COVID-19 ARDS to bacterial sepsis with ARDS
62 (herein referred to as bacterial ARDS) (Extended Fig 2b), as there were unusually low admissions to ICU
63 with viral pneumonias/ARDS during the period studied, likely due to COVID-19 public health measures.

64 Patient cohorts had comparable ages, sex, days on life support and time in hospital, but COVID-19
65 patients had broader racial diversity (Extended Fig 2c,d, Extended Data Table 1). Bacterial ARDS
66 induced significant neutrophilia, and relative thrombocytopenia compared to the near normal circulating
67 neutrophil numbers in COVID-19, while both had similar degrees of lymphopenia (Extended Fig 2e).
68 Both cohorts had comparable PaO2 / FiO2 (P/F) ratios, which is an indicator of the severity of ARDS[14],
69 but bacterial ARDS patients had significantly more kidney injury demonstrated by higher levels of serum
70 creatinine (Extended Fig 2f). We further compared families of soluble inflammatory markers (Extended
71 Fig 2g) used to distinguish prototypical states, including those identified during cytokine storm (Extended

72 Fig 2h) and cytokine release syndrome (Extended Fig 2i)[15], which demonstrated similar soluble cytokine
73 and chemokine responses between the infections. Therefore, in the context of life-threatening bacterial
74 ARDS, COVID-19 ARDS patients had normal neutrophil counts, comparable IL-6 levels, and less organ
75 failure as indicated by serum creatinine levels, all of which have been previously proposed as markers of
76 COVID disease severity[16,17]. This prompted us to further investigate immune states and composition in
77 response to COVID-19 compared to bacterial ARDS.

78 The online companion atlas (biernaskielab.ca/COVID_neutrophil) contains accessible scRNAseq data
79 performed on freshly obtained whole blood at timepoint 1 (t1, <72h after ICU admission) and at timepoint
80 2 (t2, 7 days after t1) (Fig 1a). Cellular identity was mapped to 30 immune cell types/states using a
81 UMAP projection from 21 patients and 86,935 cells (Fig 1b, Extended Figure 3a). Global magnitude of
82 gene expression was directly compared between COVID-19 and bacterial ARDS patients (Extended Data
83 Table 3), which revealed a more globally altered distribution of differential expression at t1 than at t2.
84 Altered regulation of genes was most pronounced in neutrophils at t1, with lower neutrophil gene
85 expression in COVID-19 compared to bacterial ARDS (Fig 1c; Extended Fig 3b-c). At t2, the global
86 alterations in gene expression when comparing COVID-19 to bacterial ARDS were most pronounced in
87 plasmablasts (Fig 1d; Extended Fig 3d-e). We further compared and quantified the proportions of known
88 peripheral blood cellular constituents, which highlighted significant differences in CD4 T cells, CD8 T
89 cells and NK cells (Extended Fig 3f). These data highlight that significant global differences in immune
90 cell gene expression exist between COVID-19 ARDS and bacterial ARDS.

91 **COVID-19 drives specific neutrophil maturation states.**

92 Neutrophils are a primary participant in the development of ARDS[18]; yet despite similar severity of
93 ARDS between our bacterial and COVID-19 cohorts, the numbers of circulating neutrophils from clinical
94 cell counts were significantly different (Extended Fig 2d). We hypothesized that neutrophil qualitative
95 states may be important determinants of disease. Neutrophils were subjected to velocity analysis[19,20] to
96 reconstruct maturation dynamics. Louvain clusters (Fig 1e), clinical cohort, individual patient, and

velocity length were overlayed on velocity vector fields (Extended Fig 4a-d). The proportions of distinct neutrophil states were compared at t1 and this revealed a divergent expansion of IFN^{active} neutrophils (clusters 2, 4 and 5) marked by IFITM1 expression in COVID-19, which became similar to bacterial ARDS at t7 (Fig 1f-h). Expression of IFITM1 in neutrophils from COVID-19 patients at t1 was confirmed by immunofluorescent staining for IFITM1, colocalized with S100A8/9 and typical neutrophil nuclear morphology. Relative to healthy donors, the IFN^{active} population in both COVID-19 and bacterial ARDS patients were elevated (Extended Fig 4h-k), suggesting that infections dramatically alter neutrophil dynamics and that comparing COVID-19 neutrophils to healthy neutrophils may only reveal broad features separating pathogen-challenged versus non-challenged (homeostatic) neutrophils. Hence, to map pathogen-activated neutrophils dynamics with high resolution, subsequent analyses employ principal components with top loading genes that distinguish different pathogen-activated states arising during COVID-19 and bacterial sepsis for downstream dimensionality reduction.

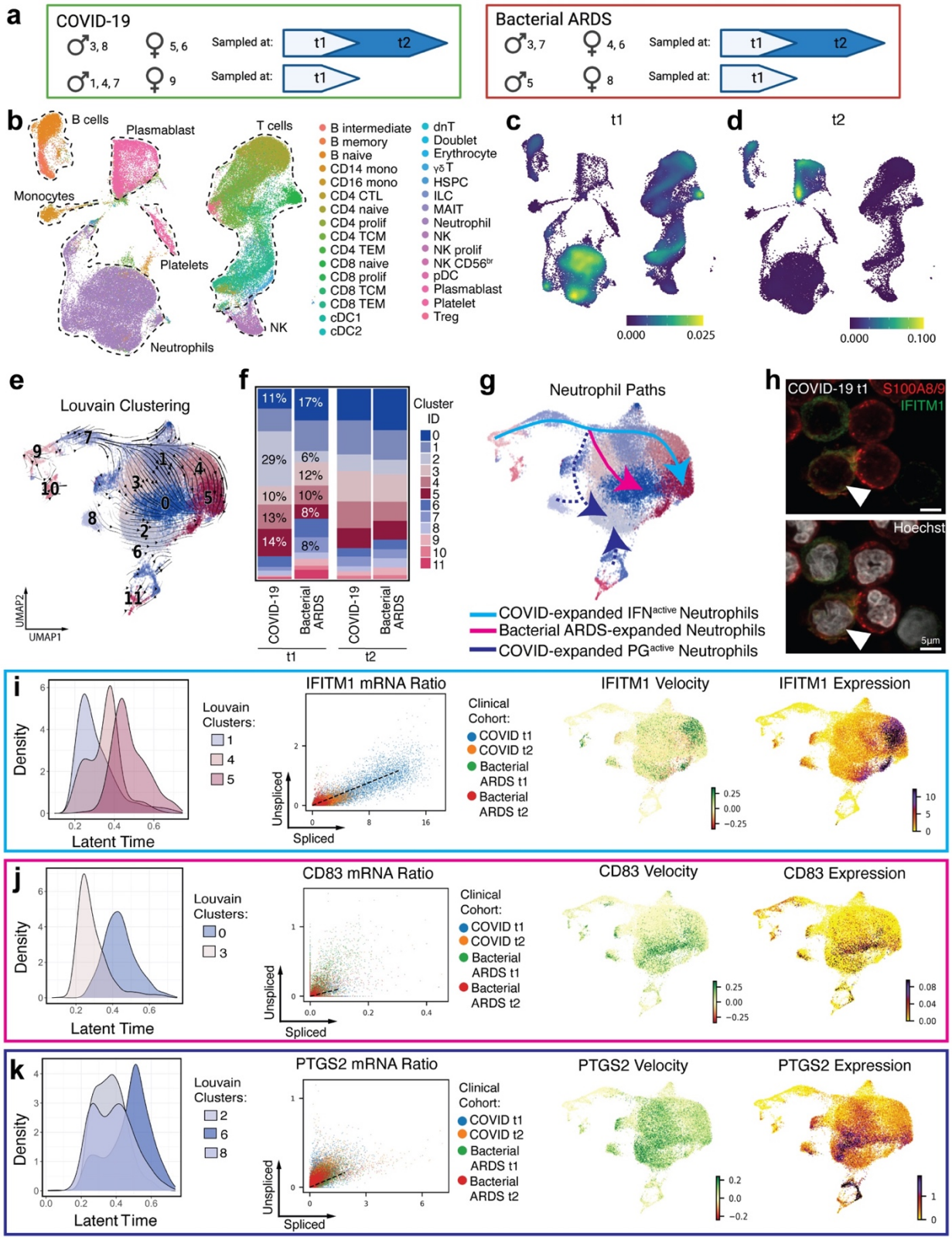

Figure 1 – COVID-19 alters neutrophil maturation. a. Schematic summarizing patients with COVID-19 and bacterial sepsis profiled at t1 and t2. **b.** UMAP projection of 86,935 whole blood cells from 21

patient samples, coloured by Azimuth reference-mapped immune cell states. **c-d.** Kernel density estimates depicting magnitude of molecular response elicited by immune cell subsets during COVID-19 compared to Bacterial ARDS at t1 (c) and t2 (d) calculated by summing DEG fold changes for each cell state shown in Panel a. **e.** UMAP plotting RNA velocity analysis of 29,653 subclustered neutrophils undergoing state transitions, coloured by cluster ID. **f.** Stacked bar plot depicting cluster composition of clinical cohorts examined. **g.** UMAP coloured by neutrophil clusters and overlaid with summary path curves based on vector fields and neutrophil state compositions in Panel d and e, respectively to determine neutrophil states. **h.** Immunocytochemistry for S100A8/A9 (red) and IFITM1 (green) expression on leukocyte-rich preparation from COVID-19 donor at tl. **i-k.** Transcriptional kinetics driving expansion of IFN^{active} (i), Bacterial ARDS-enriched (j), and PG^{active} (k) neutrophils. Latent time distribution of trajectory-associated louvain clusters (left), phase portraits with equilibrium slopes of spliced–unspliced ratios (center), and RNA velocity and gene expression (right) of selected genes driving divergent maturation trajectories. Phase portraits are coloured by clinical cohort.

Classically, peripheral neutrophils are considered terminally differentiated and non-dividing, however the increase in velocity length suggested the ability to alter phenotypic states once in circulation along specific paths or 'lineages'. COVID-19 neutrophils followed unique maturation paths compared to bacterial ARDS, culminating in three distinct terminal states: Interferon active (IFN^{active}), prostaglandin active (PG^{active}) or bacterial ARDS enriched (Fig 1e-g; Extended Fig 4e). Interestingly, the apex of this trajectory was marked by high velocity lengths, characteristic of cells undergoing differentiation (Extended Fig 4c, d). COVID-19 neutrophils preferentially transitioned from the apex of the trajectory, which was an immature state (TOP2A expressing; Extended Fig 4e) to an IFN responsive state characterized by IFITM1, IFITM2 and IFI6 expression (Cluster 1 to 4 and 5; Fig 1i; Online Atlas). This is clearly illustrated in Extended Video 1. This immature state was not present in healthy controls, though it is present in both comparator groups, suggesting these states are liberated into circulation upon pathogen exposure (Extended Fig 4h-k). The lineage relationship was less clear for COVID-19 enriched PG^{active} clusters defined by prostaglandin responsive genes (clusters 2, 6 and 8), with notable increases in PTGER4 and PTGS2 (or COX2), a proposed therapeutic target in COVID-19[21] (Fig 1k; Extended Fig 4f, g, Online Atlas). The dominant conventional bacterial ARDS state was characterized by antibacterial proteins CD83[22], CD177, and PLAC8[23] (cluster 3 to 0; Fig 1j; Online Atlas). Taken together, this data demonstrated that peripheral neutrophils have dynamic programming abilities which result in COVID-19 specific neutrophil polarization defined by the emergence of IFN^{active} and PG^{active} neutrophil states.

143 **Unique transcriptional regulatory pathways drive neutrophil maturation in COVID-19.**

144 Rapid and robust IFN responses protect against COVID-19 severe disease, while delayed responses could
145 exacerbate systemic and pulmonary inflammation[24,25]. Moreover, neutrophil IFN responses are not
146 traditionally considered during infections and neutrophils are generally considered to be homogenous,
147 with a uniform proinflammatory capacity. Global neutrophil expression aligned with neutrophil state
148 specific markers, such as interferon response genes (IFITM1, RSAD2, IFI6, and ISG10), being more
149 highly expressed in COVID-19 neutrophils (Fig 2a; Extended Fig 4f). The inverse was the case for anti-
150 bacterial proteins like PLAC8 (Fig 2a; Online Atlas). However, the discovery of differential neutrophil
151 states prompted further exploration of the factors driving neutrophil state polarization. Gene regulatory
152 network reconstruction using SCENIC analysis[26] revealed differentially activated transcription factors
153 STAT1, IRF2 and PRDM1 in COVID-19 (Fig 2b), while bacterial ARDS neutrophils had increased
154 prototypical granulocyte transcription factors such as CEBPA, CEBPB, STAT5B and less defined factors
155 such as NFE2 (Fig 2b, Online Atlas). PRDM1 activation was most pronounced in the IFN^{active} neutrophil
156 population and was likely responsible for driving expression of interferon response elements (IFIT1,
157 ISG15, IFI6) and antiviral signaling, such as RSAD2 and STAT1 (Fig 2c; Online Atlas). A hallmark of
158 PG^{active} neutrophil polarization was the activation of an E2F4 pathway (Fig 2d), while neutrophil
159 programming during bacterial ARDS included STAT5B (Fig 2e). To summarize, in response to COVID-
160 19, neutrophils were polarized by unique transcriptional regulation towards one of two main populations,
161 either an IFN^{active} population or a PG^{active} population (Fig 2f).

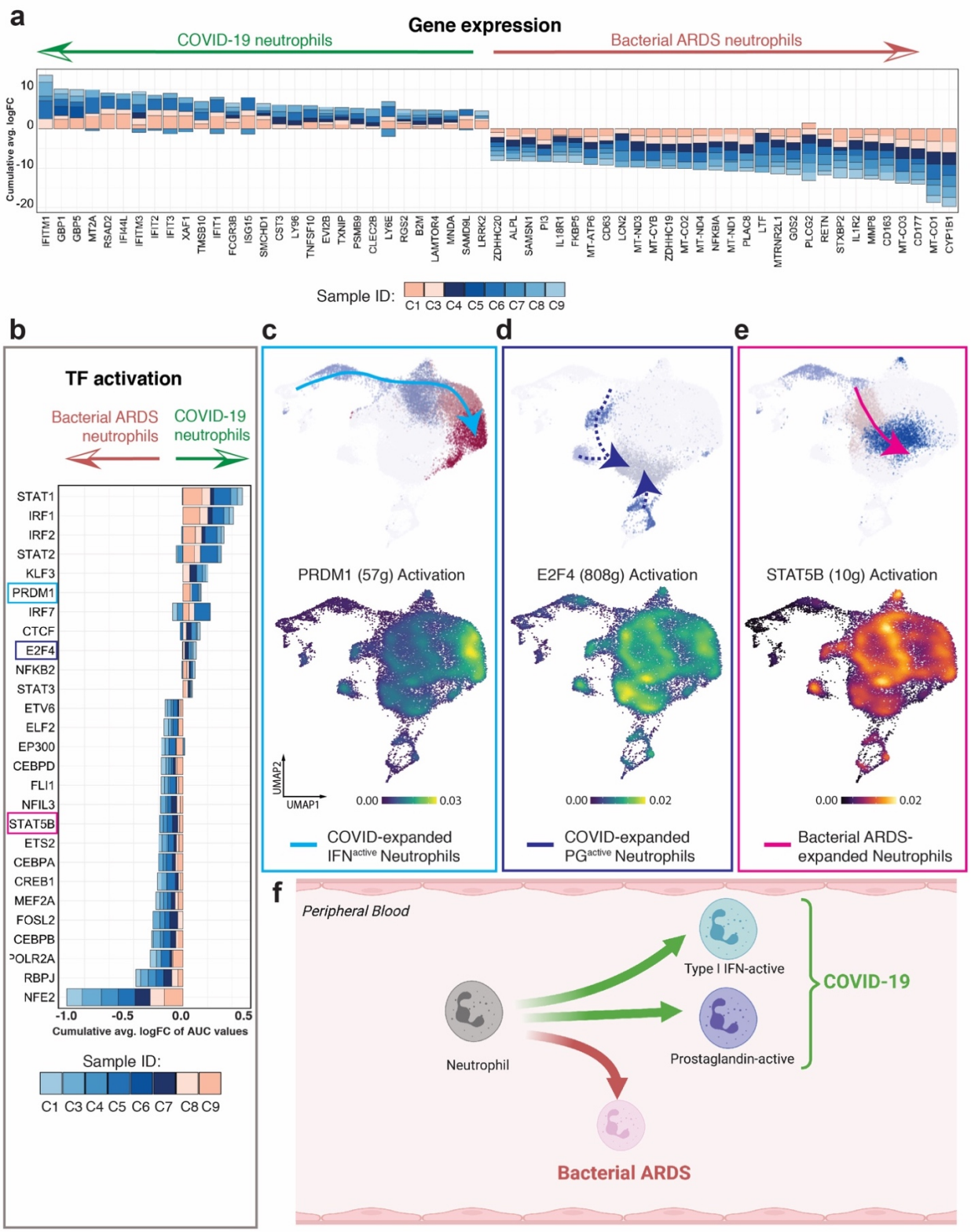

Figure 2 – Distinct regulatory programs drive divergent neutrophil maturation. a. Consensus neutrophil DEGs upregulated (positive FC) or suppressed (negative FC) during COVID-19 in at least 3 of 8 patients at t1 relative to Bacterial ARDS. **b.** Differentially activated consensus transcription factors

166 (TFs) in neutrophils from patients with COVID-19 relative to bacterial ARDS at t1. Stacked bars depict
167 logFC contributions of each COVID-19 patient. **c-e.** Gene-regulatory networks preferentially driving
168 IFN^{active} (PRDM1, c), PG^{active} (E2F4, d), and bacterial ARDS-enriched (STAT5B, e) neutrophil states.
169 Scale bars depict kernel density estimates approximating magnitude of TF activation inferred by
170 SCENIC-calculated AUCell scores. **f.** Schematic summarizing neutrophil fates favoured during COVID-
171 19 versus bacterial ARDS.

172

173 **Dexamethasone alters immune cell dynamics and plasma proteomic milieu.**

174 Conventional therapeutics have limited efficacy for COVID-19, and while dexamethasone offers a
175 moderate benefit, the RECOVERY trial reported the benefit was greatest in the most severely affected
176 patients[27]. However, the mechanisms underlying this benefit are unclear and not universal, so opportunity
177 exists to optimize or better target this therapy. In our cohort, median time between dexamethasone
178 administration to t1 blood draw (within 72 hours of ICU admission) was 31 hours (Fig 3a, Extended
179 Figure 5a, Extended Table 1). Global differences in transcription were apparent at t1 with clear
180 upregulation of genes in neutrophils and some T cell subsets in COVID-19 patients treated with
181 dexamethasone versus those that were not treated (Fig 3b-d, Extended Figure 5b, Extended Data Table 4).
182 Dexamethasone globally downregulated genes at t1, including in naïve B cells, plasmablasts and some T
183 cells (Extended Figure 5b-d). At t2 gene upregulation occurred in adaptive immune cells, including naïve
184 and effector CD8 T cells, with limited alterations in the innate myeloid cell lineages including
185 neutrophils. However, neutrophils demonstrated clear down regulation of genes at t2, as did CD4 naïve
186 and central memory T cells (Extended Figure 5e, f). Proportionally, at t1, dexamethasone administration
187 was associated with an increase in cytotoxic CD4 T cells, naïve B cells, plasmablasts, and decreased
188 proliferating NK cells, and CD4 effector memory cells (Extended Fig 5g). By t2, dexamethasone was
189 associated with suppressed neutrophil proportions in circulation compared to untreated controls (13% vs
190 41%, Extended Fig 5g). Plasma proteomics from the same cohort revealed that dexamethasone
191 suppressed 10 host proteins (S100A8, S100A9, SERPINA1, SERPINA3, ORM1, LBP, VWF, PIGR,
192 AZGP1, CRP) that others have previously identified as biomarkers distinguishing severe COVID-19
193 cases from mild to moderate counterparts (full host proteome quarriable via Online Atlas; Extended Table

194 2)[28-31]. Suppression of calprotectin (S100A8/S100A9) and neutrophil serine proteases (SERPINA1 and
195 SERPINA3), paired with depletion of neutrophil proportions, implicates the modulation of neutrophil-
196 related inflammatory processes as a method of action for dexamethasone treatment.

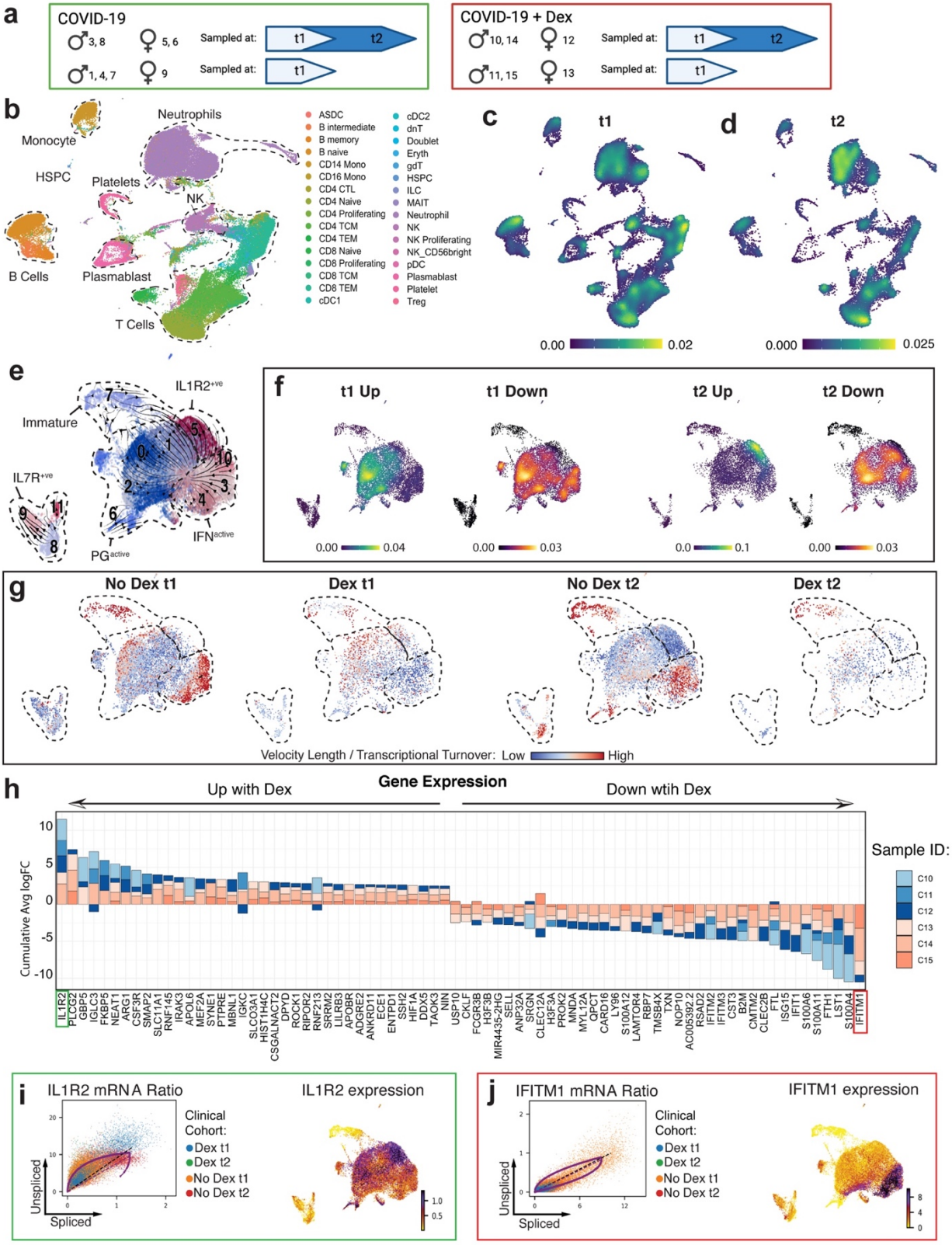
a
COVID-19
3, 8
5, 6
Sampled at:
t1
t2
1, 4, 7
9
Sampled at:
t1
COVID-19 + Dex
10, 14
12
Sampled at:
t1
t2
11, 15
13
Sampled at:
t1
b
Monocyte
Neutrophils
HSPC
Platelets
NK
B Cells
Plasmablast
T Cells
ASDC
B intermediate
B memory
B naive
CD14 Mono
CD16 Mono
CD4 CTL
CD4 Naive
CD4 Proliferating
CD4 TCM
CD4 TEM
CD8 Naive
CD8 Proliferating
CD8 TCM
CD8 TEM
cDC1
cDC2
dnT
Doublet
Eryth
gdT
HSPC
ILC
MAIT
Neutrophil
NK
NK Proliferating
NK_CD56bright
pDC
Plasmablast
Platelet
Treg
c
t1
0.00
0.02
d
t2
0.000
0.025
e
Immature
IL1R2+ve
IL7R+ve
PGactive
IFNactive
f
t1 Up
t1 Down
t2 Up
t2 Down
0.00
0.04
0.00
0.03
0.0
0.1
0.00
0.03
g
No Dex t1
Dex t1
No Dex t2
Dex t2
Velocity Length / Transcriptional Turnover: Low
High
h
Gene Expression
Up with Dex
Down wtih Dex
Cumulative Avg logFC
Sample ID:
C10
C11
C12
C13
C14
C15
IL1R2
PLCG2
GBP5
IGLC3
FKBP5
NEAT1
ARG1
CSF3R
SMAP2
SLC11A1
RNF145
IRAK3
APOL6
MEF2A
SYNE1
PTPRE
MBNL1
IGKC
SLCO3A1
HIST1H4C
CSGALNACT2
DPYD
ROCK1
RIPOR2
RNF213
SRRM2
LILRB3
APOBR
ADGRE2
ANKRD11
ECE1
ENTPD1
SSH2
HIF1A
DDX5
TAOK3
NIN
USP10
CKLF
FCGR3B
H3F3B
MIR4435-2HG
SELL
ANP32A
SRGN
CLEC12A
H3F3A
PROK2
MNDA
MYL12A
QPCT
CARD16
LY96
S100A12
LAMTOR4
RBP7
TMSB4X
TXN
NOP10
AC005392.2
RSAD2
IFITM2
IFITM3
CST3
B2M
CMTM2
CLEC2B
FTL
ISG15
IFIT1
S100A6
S100A11
FTH1
LST1
S100A4
IFITM1
i
IL1R2 mRNA Ratio
IL1R2 expression
Clinical Cohort:
Dex t1
Dex t2
No Dex t1
No Dex t2
Unspliced
Spliced
j
IFITM1 mRNA Ratio
IFITM1 expression
Clinical Cohort:
Dex t1
Dex t2
No Dex t1
No Dex t2
Unspliced
Spliced

197

198 **Figure 3 – Dexamethasone suppresses IFN programs and depletes IFN^{active} neutrophils in COVID-**
199 **19. a.** Schematic summarizing COVID-19 patients treated with or without dexamethasone profiled at t1
200 and t2. **b.** UMAP projection of 80,994 whole blood cells from 21 patient samples, coloured by Azimuth
201 reference-mapped immune cell states. **c-d.** Kernel density estimates depicting magnitude of molecular
202 response elicited by immune cell subsets following Dexamethasone treatment t1 (c) and t2 (d) calculated
203 by summing DEG fold changes for each cell state shown in Panel A. **e.** Neutrophil states overlaid on a
204 UMAP of 23,193 subclustered neutrophils from Dexamethasone- and non-Dexamethasone-treated
205 COVID-19 patients, colored by cluster ID. **f.** Magnitude of molecular response elicited by each neutrophil
206 state post-Dexamethasone treatment calculated by summing DEG fold changes for each cell state shown
207 in Panel d. **g.** RNA velocity vector length (indicating rate of differentiation/state transition) in
208 Dexamethasone- and non-Dexamethasone-treated neutrophils at t1 and t2. **h.** Consensus neutrophil DEGs
209 upregulated (positive FC) or suppressed (negative FC) post-Dexamethasone in at least 3 of 6 COVID-19
210 patients at t1 relative to non-Dexamethasone COVID-19 controls. Stacked bars depict logFC contribution
211 of each Dexamethasone-treated patient. **i-j.** Differential splicing kinetics drives activation of IL1R2 (i)
212 and suppression of IFITM1 expression (j) post-Dexamethasone treatment. Phase portraits show
213 equilibrium slopes of spliced–unspliced mRNA ratios. Green denotes most upregulated and red denotes
214 most down regulated differentially expressed genes with COVID-19 (f).

215

216 **Dexamethasone therapy restrains neutrophil IFN programs**

217 Due to the early and sustained effects of dexamethasone on gene expression in neutrophils, the effects of
218 dexamethasone therapy on neutrophil functional states were evaluated. Neutrophil reclustering again
219 identified immature neutrophils at the apex of the maturation trajectory, accelerating and exhibiting
220 maximal divergence prior to PG^{active} and IFN^{active} state commitments (Fig. 3 d, Extended Fig 6a-e).
221 Interestingly, we also identified IL7R^{+ve} neutrophils (comprising roughly 8% of total neutrophils) whose
222 trajectories remained completely separate (Fig. 3 d, Extended Fig 6g, j) suggesting an entirely distinct
223 neutrophil state. Initially, dexamethasone was associated with increased global transcription in PG^{active}
224 neutrophils, while ongoing therapy resulted in the emergence of a PG^{active} neutrophils concomitant with
225 high IL1R2 expression (IL1R2^{+ve}) (Fig. 3 e). Conversely, dexamethasone had a pronounced attenuation of
226 global transcription of IFN^{active} neutrophils at t1 and t2 (Fig 3 e, f). Remarkably, dexamethasone
227 administration at t1 halted dynamic state changes in IFN^{active} and IL7R^{+ve} neutrophils, followed by
228 preferential depletion of IFN^{active} subsets (Fig 3 g). Indeed, dexamethasone was associated with a
229 reduction in IFN^{active} neutrophils to a proportion more similar to that detected in healthy controls (9%
230 post-Dex at t2 versus 10% in healthy controls) (Fig. 4a, Extended Fig 4h-k). Although collection of
231 airway samples (i.e. bronchoalveolar lavage fluid; BALF) was not feasible at our institution, we leveraged

232 two recent BALF scRNA-Seq datasets[11,32] to assess whether IFN^{active} neutrophils dominate the
233 bronchoalveolar landscape during severe COVID-19. Projection of CSF3R^{+}S100A8^{+}S100A9^{+} BALF
234 neutrophils onto our reference revealed: a. 1.5 FC expansion of IFN^{active} neutrophils in severe COVID-19
235 relative to moderate disease (77% vs 52%, Extended Fig 7a-b), b. preferential activation of IFN-
236 stimulated genes such as IFITM1, IFITM2, IFI6, IRF7, and ISG20 in severe COVID-19 neutrophils
237 (Extended Fig 7c), and c. 4.7 FC greater IFN^{active} neutrophils in COVID-19 relative to bacterial
238 pneumonia patients (14% vs 3%, Extended Fig 7d-f). Albeit anecdotal, in our whole blood cohort, the
239 IFN^{active} neutrophil state was dominant in patient S7 [32], an 80-year-old male with remarkably high viral
240 titers who succumbed to COVID-19 complications within 3-4 days of sampling (Extended Fig 7f).

241 Consensus DEG analysis highlighted that upregulation of IL1R2, a decoy receptor that sequesters IL-1,
242 and downregulation of IFITM1 were the most prominent discriminating features of treatment with
243 steroids (Fig. 3h). Additionally, dexamethasone attenuated neutrophil expression of IFN pathways more
244 broadly, including the reduction of IFITM1-3, IFIT1, ISG15 and RSAD2 (Fig 3h). Examination of
245 unspliced pre-mRNA to mature spliced mRNA ratios supported the notion that induction of
246 immunoregulatory systems (i.e., IL-1R2; Fig 3 i) and suppression of IFN (i.e., IFITM1; Fig 3 j) programs
247 were driven by differential splicing kinetics.

248 **Dexamethasone therapy intensifies neutrophil immunosuppressive function**

249 Corticosteroid therapy shifted neutrophil state compositions. While IFN^{active} neutrophils were significantly
250 depleted by seven days of therapy, there was >2-fold expansion in immature neutrophils relative to non-
251 treated COVID-19 controls (Fig 4a; Extended Fig 6 h, i), which were absent in the healthy controls.
252 Albeit anecdotal, the dominance of IFN^{active} neutrophils at t1 in the patient who succumbed to COVID-19
253 in the non-dexamethasone cohort further supports depletion of IFN^{active} neutrophils as a mechanism by
254 which dexamethasone is protective (Extended Fig 8 g-j). Assessment of gene regulatory networks
255 demonstrated that IRF7 and MEF2A exhibited opposing activation patterns, with IRF7 being the most
256 suppressed and MEF2A the most enhanced transcription factors identified with dexamethasone, which

257 correlates with the emergence of PG^{active} and $IL1R2^{+ve}$ states and attenuation of the IFN^{active} neutrophil
258 states (Fig 4b, Extended Fig 6k-m). To assess the generalizability of the dexamethasone regulated DEGs
259 identified in our cohort, we asked whether they accurately predicted mortality due to COVID-19 in a
260 larger validation cohort. By leveraging a whole blood bulk RNA-Seq dataset from 103 COVID-19
261 patients[33 34], we scored each sample by the aggregated expression of dexamethasone suppressed DEGs at
262 t1 and t2 (Extended Data Table 3). Interestingly, suppressed DEGs at t2 (but not t1) proved to be a far
263 superior predictor of 28-day mortality (AUC: 0.78, CI: 0.67 -0.89) compared to clinical severity scales
264 such as sequential organ failure assessment (SOFA) (AUC: 0.67, CI: 0.51-0.82) across all classification
265 thresholds (Fig 4c).

266 Unexpectedly, steroid administration was associated with an increase in circulating immature neutrophils,
267 which highly expressed TOP2A, and activated ATF4 and JDP2, transcription factors seen in
268 undifferentiated cells or those undergoing nuclear reprogramming (Extended Fig 6h). Interestingly, these
269 immature neutrophils expressed high levels of ARG1, ANXA1 (Fig 4d), and CD24 (both mRNA and
270 protein; Extended Fig 6 i), also suggesting an immunomodulatory role[35,36,37-39] that was expanded with
271 dexamethasone treatment. Both ARG1 and ANXA1 express glucocorticoid response elements, supporting
272 direct regulation by dexamethasone treatment[40,41].

273 To further understand the role of neutrophils during COVID-19 and the effects of dexamethasone, we
274 investigated cellular connectomes. Cellular interactions between many cell types (including highly
275 interactive neutrophils) were noted (Extended Fig 8a), and dexamethasone altered the globally predicted
276 interactions by suppressing intercellular signalling, in both number and strength of interactions (Extended
277 Fig 8b, c). Dexamethasone enhanced (Fig 4e) and suppressed (Extended Fig 8d) a number of unique
278 neutrophil-driven signalling networks. Of note, annexin family signalling, which was enhanced in the
279 immature neutrophils and represent powerful immunomodulators, were augmented between neutrophils
280 and the other circulating immune cells when patients received dexamethasone (Fig 4e). Of note is the
281 direction of annexin family signaling, which switched from incoming toward neutrophils without

282 dexamethasone treatment to being almost entirely outgoing from neutrophils toward B intermediate and
283 memory cells and MAIT cells following dexamethasone (Fig 4f, g, Extended Fig 8e, f). Therefore,
284 dexamethasone directly altered neutrophil functional states, by promoting expansion of an
285 ARG1+/ANXA1+ immature state with immunosuppressive features and altered the global
286 communication structure such that neutrophils became active instructors of some peripheral immune
287 cells.

288 **Neutrophil response to dexamethasone is sexually dimorphic**

289 Given the apparent clinical benefit of dexamethasone is more evident in males[27], and since males are
290 predisposed to more severe COVID-19 presentations and outcomes[42] , we surmised that dexamethasone
291 incites sexually dimorphic immunosuppressive effects. Our retrospective province-wide audit comparing
292 72 pre-dexamethasone (51 M, 21 F) versus 1,581 post-dexamethasone (1013 M, 568 F) treated ICU-
293 admitted patients confirmed a preferential mortality benefit in male COVID-19 patients (Extended Fig 9a,
294 b). While dexamethasone modulated 525 neutrophil DEGs across both sexes, while 892 were uniquely
295 modulated in either males or females (Extended Data Table 5). Amongst the jointly modulated DEGs, a
296 subset (24 of 525) exhibited statistically significant dimorphism in either magnitude or direction of
297 regulation (Extended Fig 9c, d). Interestingly, while neutrophils were depleted in both sexes post-
298 dexamethasone, this was particularly pronounced in males (1.9 FC higher in males at t1 and 3.4 FC
299 higher in males at t2, Extended Fig 9e). Of the two salient neutrophil state alterations, an immature
300 ($ARG1^{+ve}$ immunosuppressive) state was preferentially expanded with dexamethasone in males (Extended
301 Fig. 9e), whereas ISGs were preferentially suppressed (Extended Fig. 9f) and IFN^{active} states were
302 depleted in females (Extended Fig. 9g-h) at both t1 and t2 (Fig 4h, i). Sexually dimorphic effects of
303 dexamethasone on neutrophil maturation kinetics may in part explain these state alterations. Dynamo-
304 reconstructed vector dynamics revealed that dexamethasone slowed IFN^{active} transitions (Extended Fig. 9i)
305 whilst accelerating immature ($ARG1^{+ve}$ immunosuppressive) neutrophil differentiation in females
306 (Extended Fig. 9j) ultimately leading to a diminished immature neutrophil progenitor pool.

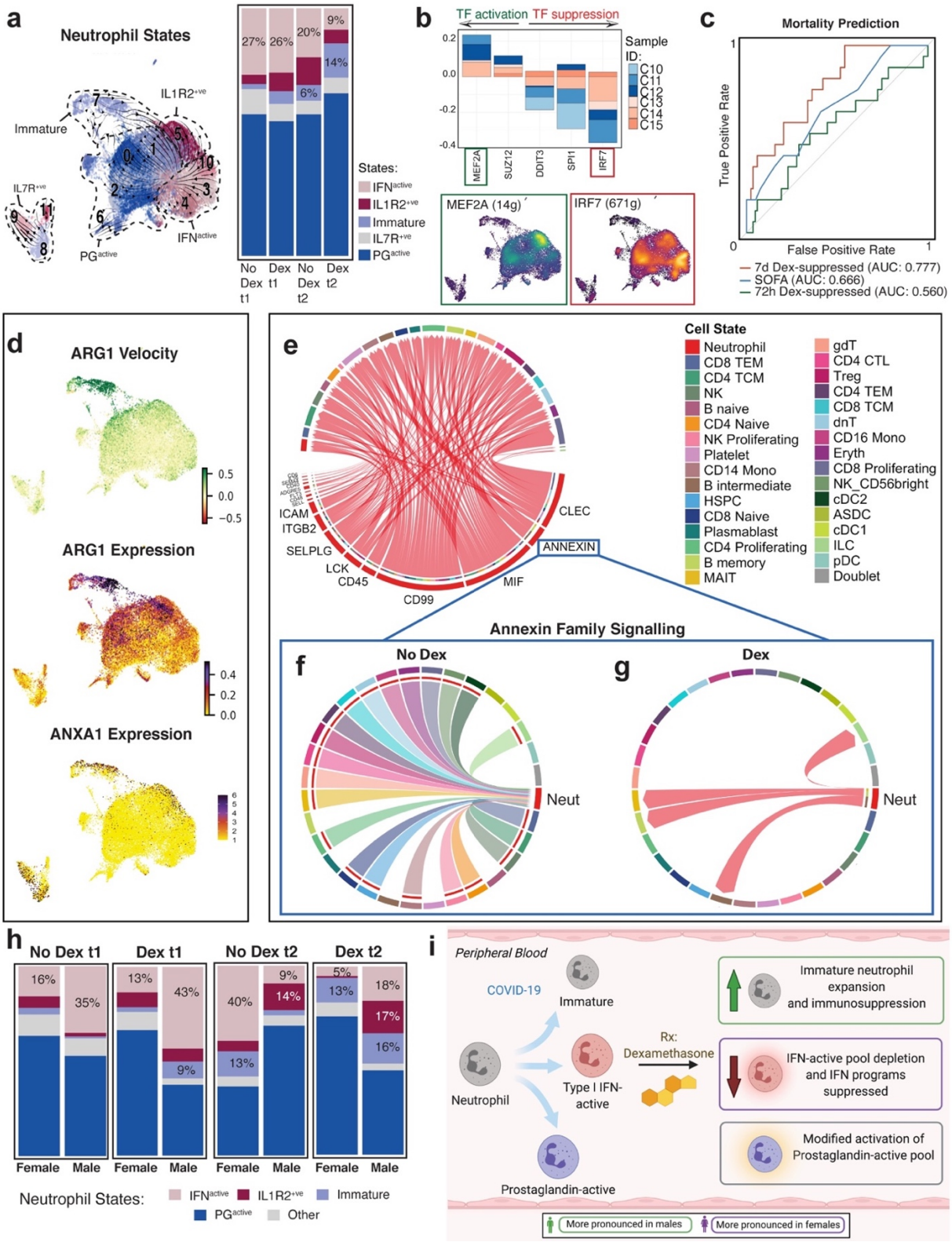

Figure 4 – Dexamethasone expands immunosuppressive neutrophils and their interactions in COVID-19. a. Neutrophil states mapped onto Louvain-clustered UMAP, with comparison of neutrophil composition between dexamethasone- and non-dexamethasone-treated samples at t1 and t2. **b.** Consensus

TFs activated or suppressed post-dexamethasone in at least 3 of 6 patients at t1 and predicted activity of MEF2A and IRF7, two of the most differentially regulated TFs post-dexamethasone. **c.** Receiver operating characteristic (ROC) curves assessing the discriminatory capacity of dexamethasone suppressed DEGs at t1, t2, and sequential organ failure assessment (SOFA) scores for predicting 28-day mortality in a validation cohort of 103 bulk whole blood RNA-Seq samples where 17 cases were fatal. **d.** Immature and IL1R2^{+ve} neutrophil subsets express high levels of immunosuppressive neutrophil marker ARG1 and ANXA1. **e.** Neutrophil-driven signaling pathways induced post-dexamethasone, identified using CellChat (MHC-I signalling filtered out). **f**, **g**. Topology of annexin signalling without (e) and with dexamethasone (f) treatment (edges filtered to those where neutrophils function as senders or recipients of annexin signals). **h.** Neutrophil state composition separated by sex and dexamethasone status at t1 and t2. **i.** Schematic summarizing the effects of dexamethasone on neutrophil fates and function in COVID-19 following dexamethasone treatment.

Conclusions

Surviving SARS-CoV-2 infection depends on striking a temporal balance between inciting viral clearance immune programs during the early stage and subsequently restraining those same programs at later stages to limit immunity-induced tissue damage. IFN signaling stands at the nexus between antiviral immunity and over active effector immune programs that inadvertently compromise tissue function and threaten survival[43]. Our work uncovered downstream IFN signalling as a signature of a stable neutrophil state that is selectively expanded during late stage COVID-19 infection from a common pool of immature progenitors. Given that inborn errors [25] and suppressed *early stage* [6] IFN signalling predicts COVID-19 severity, increased IFN^{active} neutrophils in females correlated with decreased mortality[44], and early initiation of IFN therapy has been suggested to mitigate disease severity [45,46], one may posit that IFN activity in neutrophils represents a concerted host antiviral program.

Interestingly, immunosuppression with dexamethasone, a corticosteroid known to improve mortality in hospitalized COVID-19 patients[27], was associated with suppressed COVID19-specific IFN regulatory networks and depleted COVID19-enriched IFN^{active} neutrophils in favour of expanding immature (ARG1^{+} immunosuppressive) neutrophils. These altered neutrophil states shared striking resemblances to bacterial ARDS, suggesting installation of generalized microbicidal programs ameliorate the overzealous neutrophil responses during COVID-19 (and perhaps during other viral infections). While neutrophil ISG activation may promote anti-viral immunity during early stages of SARS-CoV-2 infection, sustained IFN

342 activation during *late stages* (e.g., critically ill patients requiring intensive care) could drive
343 immunopathology of COVID-19. Indeed, positive correlation between neutrophil Type 1 IFN programs
344 and COVID-19 severity[7,47] paired with our observation that IFN^{active} neutrophils dominate the
345 bronchoalveolar microenvironment during severe COVID-19 [11]directly support this view.
346 Immunotherapies that support the innate antiviral immune response by decoupling IFN-exaggerated
347 neutrophil response whilst reinforcing acquisition of suppressor states may limit the pathogenic potential
348 of neutrophils and provide tremendous clinical benefit for treating severe COVID-19.

349 There are three major limitations of our study. First, non-random group allocation (since the timing of the
350 RECOVERY trial made dexamethasone standard of care overnight) and small sample size may
351 inadvertently introduce selection bias and limit generalizability of dexamethasone findings. Second,
352 comparisons were against bacterial ARDS, and not related respiratory viral infections (i.e., H1N1
353 influenza) since public health measures eradicated such cases; this precludes assessment of whether the
354 dynamics defined are specific to SARS-CoV-2. Finally, a subset of patients sampled at t1 were
355 discharged from ICU prior to t2 collection (non-random or non-ignorable missing data), precluding
356 unbiased estimation of temporal changes between timepoints.

357 **Methods**

358 **Patient enrolment.** All patients were enrolled following admission to any of the four adult intensive care
359 units at South Health Campus, Rockyview General Hospital, Foothills Medical Center or Peter Lougheed
360 Center in Calgary, Alberta, Canada (Extended Fig 1). Patient admission to the ICU was determined by the
361 attending ICU physician based on the need for life sustaining interventions, monitoring and life-support.
362 The research teams did not participate in clinical decisions. Study inclusion required a minimal age of 18,
363 the ability to provide consent, or for most participants, the ability of a surrogate decision maker to provide
364 regained capacity consent. All participants required an arterial catheter for blood draws, but the insertion
365 of this catheter was at the discretion of the attending medical team. Participants required a positive
366 clinical RNA COVID-19 test prior to enrolment, and evidence of bilateral lung infiltrates and hypoxemia

367 consistent with ARDS. At the time of sample collections, all COVID-19^{+} enrolled individuals were
368 culture negative for concurrent bacterial infections in the blood, urine, and sputum. The bacterial ARDS
369 cohort required a negative COVID-19 test and a definitive microbiological diagnosis of bacterial
370 pneumonia with chest imaging consistent with a diagnosis of ARDS. Patients were excluded from our
371 study if they: 1. were on immunosuppressive therapies, 2. had established autoimmune disease, or 3. had
372 active malignancy. Since tocilizumab or other immunomodulatory agents were not approved for use in
373 patients with severe COVID-19 in Alberta over the timespan of this study, none of them received these
374 medications. While bacterial sepsis patients received appropriate antibiotic treatments, none were
375 prescribed immunosuppressive or steroid therapy. All bacterial sepsis patients had lung infections caused
376 by gram-positive cocci (4 *Staphylococcus aureus* and 2 *Streptococcus pneumoniae*). Participants were
377 required to have a definitive diagnosis and appropriate consent and samples collected within 72hrs of
378 admission to the ICU in order to be included. Timepoint 1 (T1) refers to the first blood draw, while T2
379 was a repeat blood draw taken 7 days after T1, if the participant remained in the ICU, and had an arterial
380 catheter. For each participant, whole blood was collected via the arterial catheter and immediately
381 processed for analysis. Healthy blood donors were recruited by university-wide advertisement and
382 required that participants were: 1. not on immunomodulatory medications, 2. were asymptomatic for
383 SARS-CoV-2, 3. did not receive vaccination against SARS-CoV-2, and 4. did not have underlying
384 immune disorders.

385 **Epidemiological analysis.** We used the Alberta provincial eCRITICAL oracle-based analytics database
386 (Tracer) to query and extract Alberta COVID-19 ICU cases and volumes for this study[48]. Aggregate data
387 from sixteen individual adult ICUs was obtained over the study periods. The administration of
388 dexamethasone was not possible to capture at an aggregate level; therefore, we queried the database for
389 patients admitted to ICU prior to dexamethasone becoming standard of care in our Province (pre-
390 dexamethasone era; January 2020 till May 31st, 2020) versus dexamethasone as standard of care for
391 severe COVID-19 (June 1st, 2020, till May 31st, 2021). Tocilizumab was approved for use in Alberta

392 March 11 2021, and a small supply (150 doses) was obtained for severe COVID-19 patients after this
393 date.

394 **Human Study Ethics**. All work with humans was approved by the Conjoint Health Research Ethics
395 Board (CHREB) at the University of Calgary (Ethics ID: REB20-0481) and is consistent with the
396 Declaration of Helsinki.

397 **Serum cytokine assessment.** Cytokines, chemokines and soluble cytokine receptors were quantitated on
398 multiplex arrays that included a 65 MIlliPLEX cytokine/chemokine (6Ckine, BCA-1, CTACK, EGF,
399 ENA-78, Eotaxin, Eotaxin-2, Eotaxin-3, FGF-2, Flt-3L, Fractalkine, G-CSF, GM-CSF, GRO, I-309,
400 IFNα2, IFNγ, IL-1α, IL-1β, IL-1ra, IL-2, IL-3, IL-4, IL-5, IL-6, IL-7, IL-8, IL-9, IL-10, IL-12 (p40), IL-
401 12 (p70), IL-13, IL-15, IL-16, IL-17A, IL-18, IL-20, IL-21, IL-23, IL-28a, IL-33, IP-10, LIF, MCP-1,
402 MCP-2, MCP-3, MCP-4, MDC, MIP-1α, MIP-1β, MIP-1d, PDGF-AA, PDGF-AB/BB, RANTES, SDF-1
403 a+b, sCD40L, SCF,TARC, TGFa, TNFa, TNFb, TPO, TRAIL, TSLP, VEGF) and a 14 MilliPLEX
404 soluble cytokine (sCD30, sEGFR, sgp130, sIL-1RI, sIL-1RII, sIL-2Ra, sIL-4R, sIL-6R, sRAGE, sTNF
405 RI, sTNF RII, sVEGF R1, sVEGF R2, sVEGF R3) arrays (Millipore Sigma, Oakville, ON, Canada) on a
406 Luminex Model 200 Luminometer (Luminex Corporation, Austin, TX). EDTA-plasma samples were
407 collected from each patient by venipuncture following a standard operating protocol (SOP) and stored at -
408 80C until tested. Each run included a full range of calibrators. The Mann-Whitney U test was used to
409 compare groups and p-values were adjusted for multiple comparisons using Holm-Šídák stepdown
410 method with alpha set to 0.05.

411 **Shotgun proteomics using Liquid Chromatography and Mass Spectrometry (LC-MS/MS)**

412 The serum of COVID-19 patients (COVID-19 = 9, dexamethasone-treated = 4) and bacterial ARDS
413 controls (N = 6) were collected and subjected to quantitative proteomics. The total protein concentrations
414 were determined by Pierce™ BCA Protein Assay Kit (23225, ThermoFisher). A trichloroacetic acid
415 (TCA)/acetone protocol was used to pellet 100μg of proteins per sample. Samples were subjected to a

416 quantitative proteomics workflow as per supplier (Thermo Fisher) recommendations. Samples were
417 reduced in 200mM tris(2-carboxyethyl)phosphine (TCEP), for 1h at 55°C, reduced cysteines were
418 alkylated by incubation with iodoacetamide solution (50mM) for 20min at room temperature. Samples
419 were precipitated by acetone/methanol, and 600µL ice-cold acetone was added followed by incubation at
420 -20°C overnight. A protein pellet was obtained by centrifugation (8,000g, 10min, 4°C) followed by
421 acetone drying (2min). Precipitated pellet was resuspended in100 µL of 50mM triethylammonium
422 bicarbonate (TEAB) buffer followed by tryptase digestion (5µg trypsin per 100µg of protein) overnight at
423 37°C. TMT-6plex™ Isobaric Labeling Reagents (90061, Thermo Fisher) were resuspended in anhydrous
424 acetonitrile and added to each sample (41µL TMT-6plex™ per 100µL sample) and incubated at room
425 temperature for 1h. The TMT labeling reaction was quenched by 2.5% hydroxylamine for 15min at room
426 temperature. TMT labeled samples were combined and acidified in 100% trifluoroacetic acid to pH < 3.0
427 and subjected to C18 chromatography (Sep-Pak) according to manufacturer recommendations. Samples
428 were stored at -80°C before lyophilization, followed by resuspension in 1% formic acid before liquid
429 chromatography and tandem mass spectrometry analysis.

430 Tryptic peptides were analyzed on an Orbitrap Fusion Lumos Tribrid mass spectrometer (Thermo
431 Scientific) operated with Xcalibur (version 4.0.21.10) and coupled to a Thermo Scientific Easy-nLC
432 (nanoflow liquid chromatography) 1200 System. Tryptic peptides (2µg) were loaded onto a C18 trap
433 (75µm x 2cm; Acclaim PepMap 100, P/N 164946; ThermoFisher) at a flow rate of 2µL/min of solvent A
434 (0.1% formic acid in LC-MS grade H2O). Peptides were eluted using a 120min gradient from 5 to 40%
435 (5% to 28% in 105min followed by an increase to 40% B in 15min) of solvent B (0.1% formic acid in
436 80% LC-MS grade acetonitrile) at a flow rate of 0.3µL/min and separated on a C18 analytical column
437 (75µm x 50cm; PepMap RSLC C18; P/N ES803A; ThermoScientific). Peptides were then electrosprayed
438 using 2.1kV voltage into the ion transfer tube (300°C) of the Orbitrap Lumos operating in positive mode.
439 For LC-MS/MS measurements with the FAIMS Pro (Thermo Fisher Scientific), multiple compensation
440 voltages (CV) were applied, -40V, -60V, and -80V with a cycle time of 1 second. FAIMS was used to

441 generate technical replicates from plex 1 to 6. The Orbitrap first performed a full MS scan at a resolution
442 of 120,000 FWHM to detect the precursor ion having a m/z between 375 and 1,575 and a +2 to +4 charge.
443 The Orbitrap AGC (Auto Gain Control) and the maximum injection time were set at 4 x 10^5 and 50ms,
444 respectively. The Orbitrap was operated using the top speed mode with a 3 second cycle time for
445 precursor selection. The most intense precursor ions presenting a peptidic isotopic profile and having an
446 intensity threshold of at least 2 x 10^4 were isolated using the quadrupole (Isolation window (m/z) of 0.7)
447 and fragmented using HCD (38% collision energy) in the ion routing multipole. The fragment ions (MS2)
448 were analyzed in the Orbitrap at a resolution of 15,000. The AGC and the maximum injection time were
449 set at 1 x 10^5 and 105ms, respectively. The first mass for the MS2 was set at 100 to acquire the TMT
450 reporter ions. Dynamic exclusion was enabled for 45 seconds to avoid of the acquisition of same
451 precursor ion having a similar m/z (plus or minus 10ppm).

452 **Proteomic data and bioinformatics analysis**

453 Spectral data acquired from the mass spectrometer were matched to peptide sequences using MaxQuant
454 software (v.1.6.14)[49]. Due to a lack of direct compatibility with Maxquant, spectra generated using the
455 FAIMS pro was first converted to MzXML using the FAIMS MzXML Generator from the Coon's lab
456 (https://github.com/coongroup/FAIMS-MzXML-Generator). Next, peptide sequences from the human
457 proteome and Sars-CoV-2 proteins were obtained from the UniProt database (May 2021) and matched
458 using the Andromeda[50] algorithm at a peptide-spectrum match false discovery rate (FDR) of 0.05. Search
459 parameters included a mass tolerance of 20 p.p.m. for the parent ion, 0.5 Da for the fragment ion,
460 carbamidomethylation of cysteine residues (+57.021464 Da), variable N-terminal modification by
461 acetylation (+42.010565 Da), and variable methionine oxidation (+15.994915 Da). Relative quantification
462 was set as TMT 6-plex labels 126 to 131. The cleavage site specificity was set to Trypsin/P, with up to
463 two missed cleavages allowed. Next, the evidence.txt and proteinGroups.txt were loaded into the R
464 software (v4.0.2) for statistical analysis. The normalization and identification of differentially expressed

465 proteins was performed using the MSstatsTMT package[51]. Multiple comparisons were corrected using the
466 Benjamini-Hochberg approach.

467 **Leukocyte and lymphocyte isolation.** For lymphocyte isolation, whole blood (2mL) was collected in
468 5mL polystyrene round-bottom heparinized vacutubes. To isolate lymphocytes by immunomagnetic
469 negative selection, 100µL of Isolation Cocktail and 100µL of Rapid Spheres (EasySep™ Direct Human
470 Total Lymphocytes Isolation Kit: 19655, StemCell Technologies) were added to 2 mL of whole blood.
471 After mixing and 5min incubation at RT, the sample volumes were topped up to 2.5mL with 0.04%
472 bovine serum albumin (BSA) in PBS. The diluted sample was incubated in the magnet without lid for
473 5min, at RT and negatively selected lymphocytes were decanted into a new 5 mL polystyrene tube.
474 Except the addition of Isolation Cocktail, all steps were repeated once. The final lymphocyte cell
475 suspension was transferred to a 15 mL polypropylene tube and a volume of 5mL 0.04% BSA in PBS was
476 added to the sample. Lymphocytes were precipitated by centrifugation for 5 min at 2000rpm, supernatant
477 was discarded, and cells were resuspended in 5 mL of 0.04% BSA in PBS. This last step was repeated
478 once, and cells were then resuspended in 100 µL of PBS+0.04% BSA. Cell density was quantified with a
479 hemacytometer, cell viability was assessed with Trypan Blue staining (T8154; Sigma Aldrich), and 7500
480 live lymphocytes were transferred to a sterile 1.5 mL microcentrifuge tube.

481 For leukocyte isolation, 1 mL of whole blood from heparin containing vacutubes was transferred to 5 mL
482 polystyrene round-bottom tubes and 12µL of 0.5M EDTA was added. 2% FBS in PBS (1mL) and 50µL
483 of EasySep RBC Depletion spheres (EasySep™ RBC Depletion Reagent: 18170, Stem Cell
484 Technologies) were added to immunomagnetically deplete red blood cells. After 5 min of magnet
485 incubation at RT, cell suspension containing leukocytes was decanted into a new 5mL polystyrene tube.
486 To ensure complete removal of red blood cells, RBC depletion was repeated, and cell suspension
487 containing leukocytes was decanted into a new 15mL polypropylene tube. Leukocytes were precipitated
488 by centrifugation at 2000rpm for 5 min at 20ºC and resuspended in 5mL of 0.04% BSA in PBS. This last
489 step was repeated once, and leukocytes were resuspended in 2 mL of 0.04% BSA in PBS. Cell viability

490 and cell density were assessed, and 7500 live leukocytes were transferred to the microcentrifuge tube
491 containing the lymphocyte cell suspension. The volume of the cell suspension containing 7500
492 lymphocytes and 7500 leukocytes in a total of 50 μL of 0.04% BSA in PBS.

493 **Immunocytochemistry and immunohistochemistry**

494 Isolated leukocyte and lymphocyte samples were fixed in 4% paraformaldahyde in PBS (0.2mM and
495 pH7.4), and spun in a cytocentrifuge (8min at 300g) onto coated slides. Pathological lung sections (FFPE
496 fixed and sectioned at 5um) were deparaffinized in Slide Brite (Fisher Scientific NC968653) and
497 rehydrated. Slides were permeabilized and blocked with 10% normal donkey serum in PBS (with 0.5%
498 triton X-100), primary antibodies (S100A8/9 Abcam ab22506; IFITM1 Abcam ab233545) were
499 incubated at 4°C overnight, followed by incubation with donkey anti-rabbit-Alexa488 (Invitrogen
500 A32790) or anti-mouse-Alexa555 (Invitrogen A31570) for 1h at room temperature (RT). Cytospun slides
501 were sequentially stained with CD24 (Abcam ab202073) on the same slides for 1h at RT, followed by
502 donkey anti-rabbit-Alexa647 (Invitrogen A31573). Imaging was done using a VS-120 slide scanner
503 (Olympus) and high resolution image imaging was done using an SP8 spectral confocal microscope
504 (Leica). Image processing was completed in Fiji [52].

505 **Single-cell RNA-Seq library construction, alignment, and quality control.** A total of 15,000 single
506 cells (containing an equal proportion of leukocytes and lymphocytes) were loaded for partitioning using
507 10X Genomics NextGEM Gel Bead emulsions (Version 3.1). All samples were processed as per
508 manufacturer's protocol (with both PCR amplification steps run 12X). Quality control of resulting
509 libararies and quantification was performed using TapeStation D1000 ScreenTape assay (Agilent).
510 Sequencing was performed using Illumina NovaSeq S2 and SP 100 cycle dual lane flow cells over
511 multiple rounds to ensure each sample received approximately 32,000 reads per cell. Sequencing reads
512 were aligned using CellRanger 3.1.0 pipeline[53] to the standard pre-built GRCh38 reference genome.
513 Samples that passed alignment QC were aggregated into single datasets using CellRanger aggr with
514 between-sample normalization to ensure each sample received an equal number of mapped reads per cell.

515 Aggregated non-dexamethasone-treated COVID-19 (n = 12) and bacterial ARDS (n = 9) samples
516 recovered 1,872,659 cells that were sequenced to 38,410 post-normalization reads per cell. Likewise,
517 aggregated COVID-19 samples with (n = 9) or without (n = 12) dexamethasone recovered 1,748,551
518 single cells sequenced to 51,415 post-normalization reads per cell. Aggregated healthy samples recovered
519 19,816 cells, including 1,912 post-QC neutrophils (n = 5).

520 **Single-cell RNA-Seq computational analyses and workflows.** Filtered feature-barcode HDF5 matrices
521 from aggregated datasets were imported into the R package Seurat v.3.9 for normalization, scaling,
522 integration, multi-modal reference mapping, louvain clustering, dimensionality reduction, differential
523 expression analysis, and visualization [54]. Briefly, cells with abnormal transcriptional complexity (fewer
524 than 500 UMIs, greater than 25,000 UMIs, or greater than 25% of mitochondrial reads) were considered
525 artifacts and were removed from subsequent analysis. Since granulocytes have relatively low RNA
526 content (due to high levels of RNases), QC thresholds were informed by [8] as they recently defined several
527 rodent and human neutrophil subsets from scRNA-Seq samples. Cell identity was classified by mapping
528 single cell profiles to the recently published PBMC single-cell joint RNA/CITE-Seq multi-omic reference
529 [55].

530 **Annotation of neutrophil states.** Since no published reference automates granulocyte annotations,
531 neutrophil clusters were manually annotated by querying known markers (i.e. CSF3R, S100A8, S100A9,
532 MMP8, MMP9, ELANE, MPO)[56] and were corroborated using the R package SingleR[57]. Neutrophil
533 states were defined by grouping unsupervised (louvain at default resolution) subclusters based on two
534 overlapping criteria: scVelo-inferred neutrophil maturity, and 2. by corroborating gene expression and
535 SCENIC-inferred GRN signatures with previous human and rodent neutrophil scRNA-Seq studies.
536 Immature neutrophils were defined as $CD24^{+}ARG1^{+}ELANE^{+}MPO^{+}ATF4^{GRN\text{-}active}JDP2^{GRN\text{-}active}$
537 neutrophils [7,8,47,58]that were reproducibly assigned as 'root cells' in scVelo-based latent time pseudo-
538 ordering. IFN^{active} neutrophils were defined by preferential mRNA splicing (positive velocity) and
539 expression of IFN-stimulated genes such as IFITM1/2, IFIT1/2/3, ISG15/20, and IFI6/27/44/44L [6,44,59].

540 PG^{active} neutrophils were distinguished by preferential splicing of PTGS2/COX2 (as well as expression for
541 prostaglandin transport LST1) [44] and included a subset that expressed high levels of IL1β decoy receptor
542 IL1R2 [33]. Lastly, IL7R^{+} neutrophils (a small but distinct subset that maybe of thymic origin [60] expressed
543 high levels of ribosomal subunit genes (e.g. RPL5/7A/8/13/18/19/23/24/27/P0) that are highly
544 reminiscent of 'ribosomal^{hi}-specific cluster 7' identified previously [47].

545 **Statistical approach for comparing cell proportions.** To test whether cell composition was changed
546 due to infection type (COVID-19 versus Bacterial ARDS) or treatment group (dexamethasone versus
547 non-dexamethasone), a generalized linear mixed-effects model was employed where infection type and
548 treatment group were considered fixed and individual patients were considered random effect. Fitting was
549 done with Laplace approximation using the 'glmer' function in the 'lme4' R package [61] and p-values were
550 calculated using the R package 'car'. Boxplots comparing cell type composition were generated using the
551 ggplot2 package. Since a subset of patients sampled at t1 were discharged from ICU prior to t2 collection
552 (non-random or non-ignorable missing data), we limit statistical comparisons to between group
553 comparisons within one time point (e.g., COVID-19 72h vs Bacterial ARDS 72hr, dexamethasone-treated
554 72h vs non-dexamethasone-treated 72h) and do not estimate temporal differences across t1 and t2.

555 **Inferring cell communication networks.** Differential cell-cell interaction networks were reconstructed
556 using the Connectome R toolkit v0.2.2[62] and CellChat v1.0.0 [63]. Briefly, *DifferentialConnectome* queried
557 Seurat R objects housing datasets integrated by infection type and dexamethasone status to define nodes
558 and edges for downstream network analysis. Total number of interactions and interaction strengths were
559 calculated using CellChat's *compareInteractions* function. Differential edge list was passed through
560 *CircosDiff* (a wrapper around the R package 'circlize') and CellChat's *netVisual_chord_gene* to filter
561 receptor-ligand edges and generate Circos plots.

562 **Consensus DEGs and perturbation scores**. Differentially expressed genes (DEGs) were those with an
563 average log fold change (FC) greater than 0.25 (p-adjusted < 0.05) as determined by Seurat's Wilcoxon
564 rank-sum test. Consensus stacked bars showing cumulative log fold changes (colored by individual

565 sample contributions) were generated using *constructConsensus* function [7] for genes exhibiting
566 reproducible changes across patients (>3 for 72-hour comparisons, > 2 for 7-day comparisons). Gene Set
567 Enrichment analyses of consensus DEGs were performed using gProfiler's g:GOSt (p-value cutoff
568 <0.05). A cell state-specific 'perturbation score' was calculated to reflect the magnitude of response
569 elicited by factoring in number and cumulative FC of consensus DEGs. Perturbation scores were
570 visualized using Nebulosa-generated density plots [64].

571 **Constructing cellular trajectories using RNA velocity.** Analysis of neutrophil trajectories was
572 performed by realigning CellRanger count-generated BAMs with RNA velocity command-line tool [20]
573 using the *run10x* command and human (GRCh38) annotations. The output loom files containing spliced
574 and unspliced counts were combined to compare neutrophils in COVID-19 with Bacterial ARDS controls
575 and dexamethasone-treated with non-treated COVID-19 patients. For both analyses, combined looms
576 were imported into Seurat v.3.9 using the *ReadVelocity* function in SeuratWrappers v.0.2.0, normalized
577 using *SCTransform* v.0.3.2 [65], reduced and projected onto a UMAP, and exported as a .h5 file using the
578 *SaveH5Seurat* function. Counts stored in H5 files were imported, filtered, and normalized as
579 recommended in the scVelo v.0.2.1 workflow [19]. RNA velocities were estimated using stochastic and
580 dynamical models. Since both models yielded comparable results, stochastic model was used as default
581 for all subsequent analyses. Calculations stored in AnnData's metadata were exported as CSVs and kernel
582 density lines depicting Velocity-inferred latent time distribution were plotted with ggplot2 v.3.1.1.

583 **Gene Regulatory Network reconstruction.** Single-cell regulatory network inference and clustering
584 (SCENIC)[26] was employed to infer regulatory interactions between transcription factors (TFs) and their
585 targetome by calculating and pruning co-expression modules. Briefly, neutrophils were subsetted from
586 scVelo-realigned Seurat object and processed using default and recommended parameters specified in
587 SCENIC's vignette (https://github.com/aertslab/SCENIC) using the hg19 RcisTarget reference. Regulon
588 activity scores (in '3.4_regulonAUC.Rds', an output of the SCENIC workflow) were added to scVelo
589 object (using *CreateAssayObject* function) to jointly project trajectory and TF activity onto the same

590 UMAP embeddings. Consensus stacked bars showing cumulative logFC of AUCell scores for each TF
591 (colored by individual sample contributions) were generated by modifying the *constructConsensus*
592 function[7] for SCENIC assay. Targetome of TFs predicted as drivers of neutrophil states (stored in
593 '2.6_regulons_asGeneSet.Rds') was profiled using g:Profiler's functional enrichment analysis and genes
594 intersecting with the Interferon pathway were plotted using iRegulon (Cytoscape plugin)[66].

595 **Comparing scRNA-Seq findings with published datasets.** To test whether dexamethasone-suppressed
596 neutrophil genes at t1 and t2 (Extended Data Table 4) predicted COVID-19 mortality, we repurposed
597 methods described in [33] and employed whole blood bulk RNA-Seq datasets generated by [34] as a validation
598 cohort of 103 samples (where 17 were fatal). Briefly, each of the 103 samples were scored by the
599 aggregated expression of dexamethasone-suppressed neutrophil consensus genes at t1 and t2 using
600 Seurat's AddModuleScore(). Dexamethasone-suppressed module scores were used as the predictor
601 variable and 28-day mortality was used as the response variable to construct an ROC curve using pROC's
602 roc() function. To infer bronchoalveolar neutrophil composition in severe and moderate COVID-19 [11]and
603 across bacterial pneumonia and COVID-19 [32], neutrophils (CSF3R^{+}, S100A8^{+}, S100A9^{+}) captured in
604 BALF scRNA-Seq datasets were projected onto our peripheral blood reference using mutual nearest
605 neighbor anchoring (FindTransferAnchors) and identity transferring (TransferData and AddMetaData)
606 strategy implemented in Seurat v4 [54].

607 **COVID Neutrophil Atlas.** To enable intuitive exploration of single-cell datasets, a web portal
608 (http://biernaskielab.ca/covid_neutrophil or http://biernaskielab.com/covid_neutrophil) was built using
609 RShiny v1.1.0, shinyLP v.1.1.2, and shinythemes v.1.1.2 packages.

610 **Data availability.** Single cell RNA-Seq datasets are available at NCBI GEO (which automatically makes
611 SRA deposit) at the following accession: GSE157789. Single-cell datasets can be further explored on our
612 companion portal at http://biernaskielab.ca/COVID_neutrophil or
613 http://biernaskielab.com/COVID_neutrophil. Velocyto-generated LOOM files and processed R objects
614 are available for reanalysis from: http://doi.org/10.6084/m9.figshare.14330795. Whole blood bulk RNA-

615 Seq datasets employed as an independent validation cohort were downloaded from GSE157103. BALF
616 scRNA-Seq datasets from severe and moderate COVID-19 were downloaded from GSE145926.
617 Processed BALF scRNA-Seq objects from patients with bacterial pneumonia and COVID-19 (archived at
618 GSE167118) were downloaded from authors' archive: https://figshare.com/articles/dataset/_/13608734.
619 Mass spectrometry datasets will be available via PRIDE Archive (http://www.ebi.ac.uk/pride/archive), it
620 has been submitted (submission #: 1-20210702-114055) and is pending accessioning.

621 Proteomics data will be available at PRIDE (https://www.ebi.ac.uk/pride/), it has been submitted
622 (submission #: 1-20210702-114055) and is pending accessioning.

623 **Code availability.** All analyses were performed using publicly available software as described in the
624 methods section. Raw scripts are available upon request.

625 **Supplementary Information** is available for this paper.

626 **Acknowledgements**: This work was funded by a FastGrant from the Thistledown Foundation (JB and
627 BY) and Calgary Firefighters Burn Treatment Society (JB). S Sinha received CIHR Vanier, Alberta
628 Innovates, and Killam doctoral scholarships. E.L received an Alberta Children's Hospital Research
629 Institute postdoctoral fellowship. B.G.Y is a tier II Canada Research Chair in Pulmonary Immunology,
630 Inflammation and Host Defence. We acknowledge the assistance of the nurse practitioners, Charissa
631 Elton-Lacasse, Kirsten Deemer and Robert Ralph as well as the healthcare teams from the Calgary Adult
632 ICU's at South Health Campus, Rockyview General Hospital, Foothills Medical Center and Peter
633 Lougheed Center. We thank Dr. Kirsten Fiest and the ICU study coordinators Cassidy Codan, Zdenka
634 Slavikova and Olesya Dmitrieva. We acknowledge Dan Jones, Cathy Curr and the eCritical team (Alberta
635 Health Services in Alberta, Canada) for their help in data acquisition and extraction via eCritical
636 databases. Mortality predictions using dexamethasone-suppressed gene signatures were completed by
637 repurposing computational workflows kindly shared by Aaron Wilk and Dr. Catherine Blish (Stanford
638 University).

639 **Author contributions:** SS performed scRNAseq analyses, figure preparation, and co-wrote the paper.
640 NLR contributed to experimental design, performed scRNAseq experiments, figure preparation and co-
641 wrote the paper. AJ, RA, and LC performed bioinformatics and created the online atlas. EL, RF and APN
642 contributed to sample preparation and scRNAseq processing. MG and BM contributed to patient consent
643 and sample collection. LGA and AD conducted proteomics and related analyses. AB provided clinical
644 biospecimens. MJF provided serum cytokine assays. JB and BY conceived of all experiments,
645 experimental design, wrote the paper and supervised all experiments.

646 **The authors have no competing interests.**

647

648 **References:**

649 1 Matthay, M. A. *et al.* Acute respiratory distress syndrome. *Nat Rev Dis Primers* **5**, 18,
650 doi:10.1038/s41572-019-0069-0 (2019).
651 2 Wang, D. *et al.* Clinical Characteristics of 138 Hospitalized Patients With 2019 Novel
652 Coronavirus–Infected Pneumonia in Wuhan, China. *JAMA* **323**, 1061-1069,
653 doi:10.1001/jama.2020.1585 (2020).
654 3 Zhu, N. *et al.* A Novel Coronavirus from Patients with Pneumonia in China, 2019. *N Engl J Med*
655 **382**, 727-733, doi:10.1056/NEJMoa2001017 (2020).
656 4 Middleton, E. A. *et al.* Neutrophil extracellular traps contribute to immunothrombosis in COVID-
657 19 acute respiratory distress syndrome. *Blood* **136**, 1169-1179, doi:10.1182/blood.2020007008
658 (2020).
659 5 Veras, F. P. *et al.* SARS-CoV-2-triggered neutrophil extracellular traps mediate COVID-19
660 pathology. *J Exp Med* **217**, doi:10.1084/jem.20201129 (2020).
661 6 Combes, A. J. *et al.* Global absence and targeting of protective immune states in severe COVID-
662 19. *Nature*, doi:10.1038/s41586-021-03234-7 (2021).
663 7 Wilk, A. J. *et al.* A single-cell atlas of the peripheral immune response in patients with severe
664 COVID-19. *Nat Med* **26**, 1070-1076, doi:10.1038/s41591-020-0944-y (2020).
665 8 Xie, X. *et al.* Single-cell transcriptome profiling reveals neutrophil heterogeneity in homeostasis
666 and infection. *Nature Immunology* **21**, 1119-1133, doi:10.1038/s41590-020-0736-z (2020).
667 9 Lee, J. S. *et al.* Immunophenotyping of COVID-19 and influenza highlights the role of type I
668 interferons in development of severe COVID-19. *Science Immunology* **5**, eabd1554,
669 doi:10.1126/sciimmunol.abd1554 (2020).
670 10 Xu, G. *et al.* The differential immune responses to COVID-19 in peripheral and lung revealed by
671 single-cell RNA sequencing. *Cell Discovery* **6**, 73, doi:10.1038/s41421-020-00225-2 (2020).
672 11 Liao, M. *et al.* Single-cell landscape of bronchoalveolar immune cells in patients with COVID-19.
673 *Nature Medicine* **26**, 842-844, doi:10.1038/s41591-020-0901-9 (2020).
674 12 Wauters, E. *et al.* Discriminating mild from critical COVID-19 by innate and adaptive immune
675 single-cell profiling of bronchoalveolar lavages. *Cell Research* **31**, 272-290, doi:10.1038/s41422-
676 020-00455-9 (2021).
677 13 Rosin, N. L. *et al.* SARS-CoV-2 infection of circulating immune cells is not responsible for virus
678 dissemination in severe COVID-19 patients. *bioRxiv*, 2021.2001.2019.427282,
679 doi:10.1101/2021.01.19.427282 (2021).
680 14 Ranieri, V. M. *et al.* Acute respiratory distress syndrome: the Berlin Definition. *JAMA* **307**, 2526-
681 2533, doi:10.1001/jama.2012.5669 (2012).
682 15 Mehta, P. *et al.* COVID-19: consider cytokine storm syndromes and immunosuppression. *Lancet*
683 **395**, 1033-1034, doi:10.1016/s0140-6736(20)30628-0 (2020).
684 16 Feng, Z. *et al.* Early prediction of disease progression in COVID-19 pneumonia patients with
685 chest CT and clinical characteristics. *Nat Commun* **11**, 4968, doi:10.1038/s41467-020-18786-x
686 (2020).
687 17 Wu, C. *et al.* Risk Factors Associated With Acute Respiratory Distress Syndrome and Death in
688 Patients With Coronavirus Disease 2019 Pneumonia in Wuhan, China. *JAMA Intern Med*,
689 doi:10.1001/jamainternmed.2020.0994 (2020).
690 18 Barnes, B. J. *et al.* Targeting potential drivers of COVID-19: Neutrophil extracellular traps. *J Exp*
691 *Med* **217**, doi:10.1084/jem.20200652 (2020).
692 19 Bergen, V., Lange, M., Peidli, S., Wolf, F. A. & Theis, F. J. Generalizing RNA velocity to transient
693 cell states through dynamical modeling. *Nature Biotechnology* **38**, 1408-1414,
694 doi:10.1038/s41587-020-0591-3 (2020).

20 La Manno, G. *et al.* RNA velocity of single cells. *Nature* **560**, 494-498, doi:10.1038/s41586-018-0414-6 (2018).
21 Chen, J. S. *et al.* Non-steroidal anti-inflammatory drugs dampen the cytokine and antibody response to SARS-CoV-2 infection. *Journal of Virology*, JVI.00014-00021, doi:10.1128/JVI.00014-21 (2021).
22 Takashima, A. & Yao, Y. Neutrophil plasticity: acquisition of phenotype and functionality of antigen-presenting cell. *J Leukoc Biol*, doi:10.1189/jlb.1MR1014-502R (2015).
23 Ledford, J. G., Kovarova, M. & Koller, B. H. Impaired Host Defense in Mice Lacking ONZIN. *The Journal of Immunology* **178**, 5132, doi:10.4049/jimmunol.178.8.5132 (2007).
24 Zhang, Q. *et al.* in *Med (N Y)* Vol. 1 14-20 (© 2020 Elsevier Inc., 2020).
25 Zhang, Q. *et al.* Inborn errors of type I IFN immunity in patients with life-threatening COVID-19. *Science* **370**, doi:10.1126/science.abd4570 (2020).
26 Aibar, S. *et al.* SCENIC: single-cell regulatory network inference and clustering. *Nat Methods* **14**, 1083-1086, doi:10.1038/nmeth.4463 (2017).
27 Horby, P. *et al.* Dexamethasone in Hospitalized Patients with Covid-19 - Preliminary Report. *N Engl J Med*, doi:10.1056/NEJMoa2021436 (2020).
28 Mahler, M., Meroni, P. L., Infantino, M., Buhler, K. A. & Fritzler, M. J. Circulating Calprotectin as a Biomarker of COVID-19 Severity. *Expert Rev Clin Immunol* **17**, 431-443, doi:10.1080/1744666X.2021.1905526 (2021).
29 Demichev, V. *et al.* A time-resolved proteomic and prognostic map of COVID-19. *Cell Syst*, doi:10.1016/j.cels.2021.05.005 (2021).
30 Park, J. *et al.* In-depth blood proteome profiling analysis revealed distinct functional characteristics of plasma proteins between severe and non-severe COVID-19 patients. *Sci Rep* **10**, 22418, doi:10.1038/s41598-020-80120-8 (2020).
31 Shu, T. *et al.* Plasma Proteomics Identify Biomarkers and Pathogenesis of COVID-19. *Immunity* **53**, 1108-1122 e1105, doi:10.1016/j.immuni.2020.10.008 (2020).
32 Zhao, Y. *et al.* Clonal expansion and activation of tissue-resident memory-like T_H17 cells expressing GM-CSF in the lungs of patients with severe COVID-19. *Science Immunology* **6**, eabf6692, doi:10.1126/sciimmunol.abf6692 (2021).
33 Wilk, A. J. *et al.* Multi-omic profiling reveals widespread dysregulation of innate immunity and hematopoiesis in COVID-19. *Journal of Experimental Medicine* **218**, doi:10.1084/jem.20210582 (2021).
34 Overmyer, K. A. *et al.* Large-Scale Multi-omic Analysis of COVID-19 Severity. *Cell Systems* **12**, 23-40.e27, doi:https://doi.org/10.1016/j.cels.2020.10.003 (2021).
35 Vago, J. P. *et al.* Annexin A1 modulates natural and glucocorticoid-induced resolution of inflammation by enhancing neutrophil apoptosis. *Journal of Leukocyte Biology* **92**, 249-258, doi:https://doi.org/10.1189/jlb.0112008 (2012).
36 Oliveira, L. G. *et al.* Annexin A1 Is Involved in the Resolution of Inflammatory Responses during Leishmania braziliensis Infection. *The Journal of Immunology* **198**, 3227, doi:10.4049/jimmunol.1602028 (2017).
37 Uhel, F. *et al.* Early Expansion of Circulating Granulocytic Myeloid-derived Suppressor Cells Predicts Development of Nosocomial Infections in Patients with Sepsis. *Am J Respir Crit Care Med* **196**, 315-327, doi:10.1164/rccm.201606-1143OC (2017).
38 Arlauckas, S. P. *et al.* Arg1 expression defines immunosuppressive subsets of tumor-associated macrophages. *Theranostics* **8**, 5842-5854, doi:10.7150/thno.26888 (2018).
39 Derakhshani, A. *et al.* Arginase 1 (Arg1) as an Up-Regulated Gene in COVID-19 Patients: A Promising Marker in COVID-19 Immunopathy. *J Clin Med* **10**, doi:10.3390/jcm10051051 (2021).

742 40 Kelly-Scumpia, K. M. *et al.* ER Stress Regulates Immunosuppressive Function of Myeloid Derived
743 Suppressor Cells in Leprosy that Can Be Overcome in the Presence of IFN-γ. *iScience* **23**, 101050,
744 doi:https://doi.org/10.1016/j.isci.2020.101050 (2020).
745 41 Okun, J. G. *et al.* Molecular regulation of urea cycle function by the liver glucocorticoid receptor.
746 *Mol Metab* **4**, 732-740, doi:10.1016/j.molmet.2015.07.006 (2015).
747 42 Peckham, H. *et al.* Male sex identified by global COVID-19 meta-analysis as a risk factor for death
748 and ITU admission. *Nature Communications* **11**, 6317, doi:10.1038/s41467-020-19741-6 (2020).
749 43 Park, A. & Iwasaki, A. Type I and Type III Interferons - Induction, Signaling, Evasion, and
750 Application to Combat COVID-19. *Cell host & microbe* **27**, 870-878,
751 doi:10.1016/j.chom.2020.05.008 (2020).
752 44 Gupta, S. *et al.* Sex differences in neutrophil biology modulate response to type I interferons and
753 immunometabolism. *Proceedings of the National Academy of Sciences* **117**, 16481,
754 doi:10.1073/pnas.2003603117 (2020).
755 45 Monk, P. D. *et al.* Safety and efficacy of inhaled nebulised interferon beta-1a (SNG001) for
756 treatment of SARS-CoV-2 infection: a randomised, double-blind, placebo-controlled, phase 2
757 trial. *The Lancet Respiratory Medicine* **9**, 196-206, doi:10.1016/S2213-2600(20)30511-7 (2021).
758 46 Wang, N. *et al.* Retrospective Multicenter Cohort Study Shows Early Interferon Therapy Is
759 Associated with Favorable Clinical Responses in COVID-19 Patients. *Cell Host & Microbe* **28**, 455-
760 464.e452, doi:https://doi.org/10.1016/j.chom.2020.07.005 (2020).
761 47 Schulte-Schrepping, J. *et al.* Severe COVID-19 Is Marked by a Dysregulated Myeloid Cell
762 Compartment. *Cell* **182**, 1419-1440.e1423, doi:10.1016/j.cell.2020.08.001 (2020).
763 48 Brundin-Mather, R. *et al.* Secondary EMR data for quality improvement and research: A
764 comparison of manual and electronic data collection from an integrated critical care electronic
765 medical record system. *J Crit Care* **47**, 295-301, doi:10.1016/j.jcrc.2018.07.021 (2018).
766 49 Cox, J. & Mann, M. MaxQuant enables high peptide identification rates, individualized p.p.b.-
767 range mass accuracies and proteome-wide protein quantification. *Nat Biotechnol* **26**, 1367-
768 1372, doi:10.1038/nbt.1511 (2008).
769 50 Cox, J. *et al.* Andromeda: a peptide search engine integrated into the MaxQuant environment. *J*
770 *Proteome Res* **10**, 1794-1805, doi:10.1021/pr101065j (2011).
771 51 Huang, T. *et al.* MSstatsTMT: Statistical Detection of Differentially Abundant Proteins in
772 Experiments with Isobaric Labeling and Multiple Mixtures. *Mol Cell Proteomics* **19**, 1706-1723,
773 doi:10.1074/mcp.RA120.002105 (2020).
774 52 Schindelin, J. *et al.* Fiji: an open-source platform for biological-image analysis. *Nature Methods* **9**,
775 676-682, doi:10.1038/nmeth.2019 (2012).
776 53 Zheng, G. X. Y. *et al.* Massively parallel digital transcriptional profiling of single cells. *Nature*
777 *Communications* **8**, 14049, doi:10.1038/ncomms14049 (2017).
778 54 Stuart, T. *et al.* Comprehensive Integration of Single-Cell Data. *Cell* **177**, 1888-1902.e1821,
779 doi:https://doi.org/10.1016/j.cell.2019.05.031 (2019).
780 55 Hao, Y. *et al.* Integrated analysis of multimodal single-cell data. *bioRxiv*, 2020.2010.2012.335331,
781 doi:10.1101/2020.10.12.335331 (2020).
782 56 Zilionis, R. *et al.* Single-Cell Transcriptomics of Human and Mouse Lung Cancers Reveals
783 Conserved Myeloid Populations across Individuals and Species. *Immunity* **50**, 1317-1334.e1310,
784 doi:https://doi.org/10.1016/j.immuni.2019.03.009 (2019).
785 57 Aran, D. *et al.* Reference-based analysis of lung single-cell sequencing reveals a transitional
786 profibrotic macrophage. *Nature Immunology* **20**, 163-172, doi:10.1038/s41590-018-0276-y
787 (2019).
788 58 Reusch, N. *et al.* Neutrophils in COVID-19. *Frontiers in immunology* **12**, 652470-652470,
789 doi:10.3389/fimmu.2021.652470 (2021).

59 Shaath, H., Vishnubalaji, R., Elkord, E. & Alajez, N. M. Single-Cell Transcriptome Analysis Highlights a Role for Neutrophils and Inflammatory Macrophages in the Pathogenesis of Severe COVID-19. *Cells* **9**, doi:10.3390/cells9112374 (2020).

60 Schlenner, S. M. *et al.* Fate Mapping Reveals Separate Origins of T Cells and Myeloid Lineages in the Thymus. *Immunity* **32**, 426-436, doi:https://doi.org/10.1016/j.immuni.2010.03.005 (2010).

61 Bates, D., Mächler, M., Bolker, B. & Walker, S. Fitting Linear Mixed-Effects Models Using lme4. *Journal of Statistical Software; Vol 1, Issue 1 (2015)*, doi:10.18637/jss.v067.i01 (2015).

62 Raredon, M. S. B. *et al.* Connectome: computation and visualization of cell-cell signaling topologies in single-cell systems data. *bioRxiv*, 2021.2001.2021.427529, doi:10.1101/2021.01.21.427529 (2021).

63 Jin, S. *et al.* Inference and analysis of cell-cell communication using CellChat. *Nature Communications* **12**, 1088, doi:10.1038/s41467-021-21246-9 (2021).

64 Alquicira-Hernandez, J. & Powell, J. E. Nebulosa recovers single-cell gene expression signals by kernel density estimation. *Bioinformatics*, doi:10.1093/bioinformatics/btab003 (2021).

65 Hafemeister, C. & Satija, R. Normalization and variance stabilization of single-cell RNA-seq data using regularized negative binomial regression. *Genome Biology* **20**, 296, doi:10.1186/s13059-019-1874-1 (2019).

66 Janky, R. s. *et al.* iRegulon: From a Gene List to a Gene Regulatory Network Using Large Motif and Track Collections. *PLOS Computational Biology* **10**, e1003731, doi:10.1371/journal.pcbi.1003731 (2014).